

Research Article www.acsami.org

# Nanostructuring Enables Greatly Suppressed Thermal Conductivity and Enhanced Thermoelectric Performance in Topological Insulator Thin Films

Neil Ghosh, Yong P. Chen, and Xianfan Xu\*



Cite This: https://doi.org/10.1021/acsami.5c14518



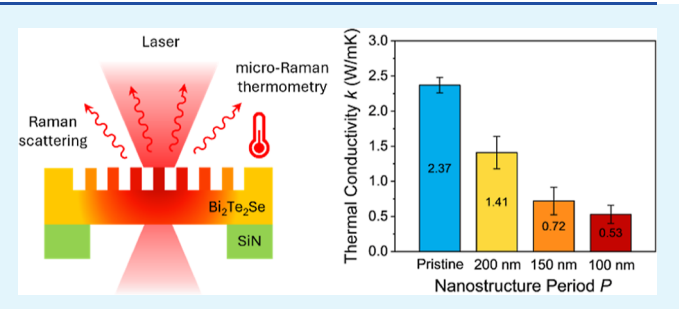
ACCESS I

Metrics & More

Article Recommendations

Supporting Information

ABSTRACT: Topological insulators (TIs) have attracted tremendous interest in the context of thermoelectrics (TE) as they are often composed of materials used for making effective and practical TE devices, while their exotic surface state electronic structures can be a promising candidate for decoupling thermal and electrical transport. However, common strategies used to improve TE performance such as using superlattices, heterostructures or alloying can often obscure the prominence of the unique properties of the topological surface states in TIs. Furthermore, obtaining a large enhancement in the TE performance in extremely thin films



of these materials, required for cooling of these thin films, along with precise experimental demonstrations of the coexisting and distinct contributions of the bulk and surface states to the TE transport, still remains a challenging task. In this work, we engineer low-dimensional nanostructures onto thin TI films to drastically improve their TE performance while retaining their unique topological surface state properties. We demonstrate a large suppression of thermal conductivity, by nearly an order of magnitude, in a thin nanostructured Bi<sub>2</sub>Te<sub>2</sub>Se film without significantly affecting its electrical conductivity. The measured thermal conductivity of nanostructured TI films is lower than other reported values for thin film TIs and approaches the amorphous limit, indicating highly disordered thermal transport. This results in an enhancement in the figure-of-merit zT by a factor  $\sim 11$  times than that of pristine thin  $Bi_2Te_2Se$  films at room temperature. The zT can be further enhanced using optical helicity-dependent control over the transport of the surface state electrons due to their unique spin-orbit coupling. The obtained zT is higher than values reported in other thin film TIs, positioning our Bi<sub>2</sub>Te<sub>2</sub>Se system as a promising alternative to more complex structures and materials. Additionally, we investigate the importance of the relative contribution of the surface states and the bulk to TE transport which points out the directions of further improvement of TE properties. Overall, this study provides critical experimental insights for developing highperformance TE materials utilizing the unique properties of thin film TIs combined with the benefits of nanostructuring.

KEYWORDS: topological insulator, thermoelectric, nanostructures, thermal conductivity, circular photogalvanic effect, helium ion beam

## **■ INTRODUCTION**

Thermoelectric (TE) materials have emerged as a promising frontier for sustainable energy harvesting and recovery due to their ability to directly and reversibly convert heat to electricity. 1,2 For developing a high-performance TE device, it is essential to simultaneously maintain a large potential and temperature gradient across its terminals while minimizing Joule heating. The performance of a TE material is quantified by its dimensionless figure-of-merit  $zT = S^2 \sigma T/k$ , where S = $\Delta V/\Delta T$  is defined as the Seebeck coefficient, T is the absolute temperature, and  $\sigma$  and k are the electrical and thermal conductivity, respectively. The total thermal conductivity k can be represented as the sum of the individual contributions from the electrons  $k_{\rm e}$  and the lattice or phonons  $k_{\rm ph}$ . The task of achieving a high zT has remained a challenge for decades as these TE parameters that need to be optimized are often intertwined and cannot be tuned independently.<sup>3</sup>

Some common strategies that have been successfully employed to improve zT include searching for intrinsically low thermal conductivity materials, 4-6 optimizing carrier concentration, <sup>7,8</sup> tuning effective mass, <sup>9</sup> band structure engineering, <sup>10,11</sup> and using materials with negatively correlated TE properties. 12 Nanostructured and heterostructured materials have emerged as another effective approach to improve TE performance over their bulk counterparts 13,14 through mechanisms such as quantum confinement, 15,16 suppressed phonon transport via increased boundary or interface

July 22, 2025 Received: Revised: November 5, 2025 Accepted: November 9, 2025



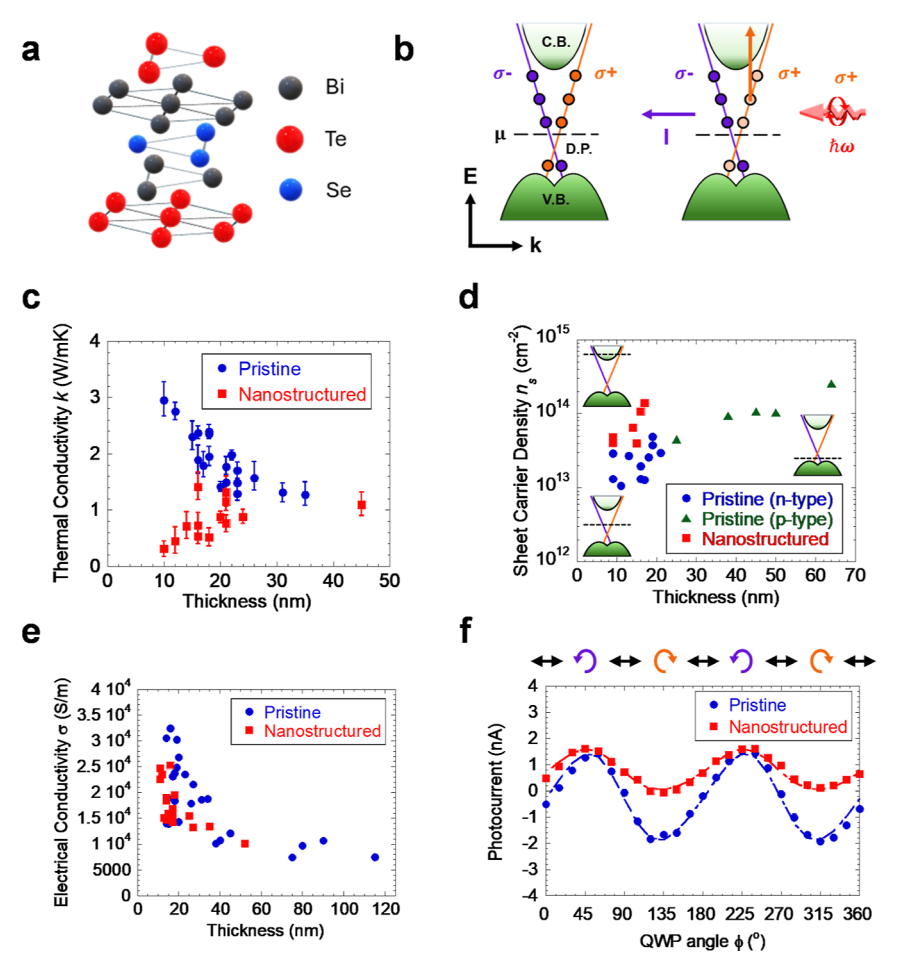


Figure 1. Thermoelectric transport in pristine and nanostructured  $Bi_2Te_2Se$  films. (a) Hexagonal crystal structure of  $Bi_2Te_2Se$  quintuple layers. (b) Schematic of energy dispersion of  $Bi_2Te_2Se$ . A net spin-polarized current can be generated by exciting the surface state electrons using circular-polarized light. (c) Thickness dependent in-plane thermal conductivity k of suspended films measured using micro-Raman thermometry. (d) Thickness dependent sheet carrier density  $n_s$  extracted from Hall effect measurements. Films thinner than 20 nm show n-type behavior while thicker films are p-type. The inset schematics illustrate the location of the chemical potential relative to the bulk bands and the Dirac point. (e) Thickness dependent electrical conductivity  $\sigma$  measured using the standard four-probe method. (f) Generated photocurrent as a function of light polarization when a 632.8 nm laser incident at  $\theta = 45^{\circ}$  is focused on the center of a 10 nm thick  $Bi_2Te_2Se$  device before and after fabricating the nanostructures. All measurements were performed at room temperature and  $V_G = 0$  V.

scattering,  $^{17,18}$  and selective filtering of charge carriers based on their mean free path or energies.  $^{19,20}$ 

Topological insulators (TI) have attracted tremendous interest in condensed matter physics due to the presence of gapless metallic states at their surface along with gapped states in the bulk.<sup>21,22</sup> The topological surface states (TSS) are immune to backscattering from nonmagnetic defects as they are protected by time-reversal symmetry, 23,24 leading to a possibility of a higher relaxation time and enhanced electrical conductivity. On the other hand, to obtain a high Seebeck coefficient, the Fermi level in the TI needs to be located near the edge of the bulk bands due to the sharp change of electron density of states. 11 Hence, the coexisting distinct properties of the TSS and the bulk states allow the possibility of tuning the TE properties of the TI by altering their relative contribution to the transport.<sup>25–27</sup> Some TIs are also composed of materials for making effective TE devices that can lead to low thermal conductivity (in part due to heavy elements), small effective mass, narrow band gaps, and complex band structures.<sup>28-30</sup> For example, some three-dimensional TI materials, including  $Bi_2Te_3$ ,  $Bi_2Se_3$ , and  $Sb_2Te_3$  and their alloys are known to be among the best TE materials. However, demonstration

of high TE performance in very thin TI films where the surface state effect dominates, at room temperature, is still lacking. Due to the unique properties of surface state, TIs combined with the benefits of nanostructuring (which can effectively reduce the contributions of bulk and thermal transport relative to the surface and electrical transport) have been theoretically predicted to be very promising candidates to decouple TE transport and realize high-performance TE materials. <sup>26,33,34</sup> However, fabrication of nanostructures on TIs without degrading their unique surface properties along with precise experimental measurements of the bulk and surface contributions to the TE properties in such systems, particularly in extremely thin TI films, remains a challenging task. <sup>25,30</sup>

In this study, we report the experimental measurements of TE properties and a substantially enhanced zT of nanostructured thin  $\mathrm{Bi_2Te_2Se}$  films. The in-plane thermal conductivity of the films is measured at room temperature using micro-Raman thermometry, a technique that has been widely used to measure the thermal properties of 2D materials. We demonstrate that a 10 nm thick nanostructured  $\mathrm{Bi_2Te_2Se}$  film has a significantly suppressed thermal conductivity of 0.31 W/mK, which is nearly an order of

magnitude lower compared to the measured value of a pristine film of the same thickness. This measured in-plane thermal conductivity at room temperature in the nanostructured film is lower than experimentally reported values for other TI thin films<sup>39-41</sup> and is also comparable to the minimum lattice thermal conductivity  $(k_{\min})$  predicted for similar materials in the amorphous limit  $^{42}$  (in-plane  $k_{\min} = 0.28$  W/mK for Bi<sub>2</sub>Te<sub>3</sub><sup>31</sup>). Crucially, this suppression in thermal transport can be achieved without significant deterioration of electrical conductivity and Seebeck coefficient. This results in a greatly enhanced zT of 0.42 in the nanostructured film, a factor  $\sim$ 11 times larger than the pristine film at room temperature. We also demonstrate that the nanostructuring of the Bi<sub>2</sub>Te<sub>2</sub>Se film does not impair its TSS by generating an additional spinpolarized electrical current using optical spin injection. This spin-polarized current originates from the TSS 43,44 and is parallel to the current driven by the temperature gradient, resulting in an enhanced apparent Seebeck coefficient and a further improved zT of 0.50 at room temperature. This obtained zT is higher than reported values for other nanostructured thin TI films. 40,45,46 Another crucial finding is the improvement of TE performance while preserving TSS properties as other common strategies used to improve TE performance like alloying or complex heterostructuring may often overshadow or hinder the peculiar properties of the TSS in TIs. 47,48 The preservation of TSS properties enables the use of the nanostructured Bi<sub>2</sub>Te<sub>2</sub>Se films for a variety of photonic and spintronics applications. 49,50 These results highlight the potential for using thin TI film itself for cooling of the TI devices, which also allows the possibility of optical modulation and on-chip active thermal management in nanoscale TI electronics.

#### RESULTS AND DISCUSSION

For measuring TE properties of Bi<sub>2</sub>Te<sub>2</sub>Se, thin films were prepared via tape exfoliation from bulk crystals. A schematic of the layered crystal structure of Bi<sub>2</sub>Te<sub>2</sub>Se is illustrated in Figure 1a. Bi<sub>2</sub>Te<sub>2</sub>Se was chosen for our experiments as compared to other widely studied three-dimensional TIs such as Bi<sub>2</sub>Te<sub>3</sub> and Bi<sub>2</sub>Se<sub>3</sub> since Bi<sub>2</sub>Te<sub>2</sub>Se has a significantly reduced electrical conduction in the bulk and is thus a better candidate for analyzing the surface state contribution to the TE transport. This is because the chemical potential  $(\mu)$  in Bi<sub>2</sub>Te<sub>2</sub>Se is located near the middle of the bulk band gap and close to the Dirac point (D.P.), as illustrated in Figure 1b, which leads to better bulk-insulating properties. Earlier ARPES, electrical transport, and Seebeck measurements performed on the bulk crystals also indicate excellent qualities of the crystals and the potential of the TSS to make significant contributions to the measured properties.<sup>53</sup> Figure 1b also illustrates the generation of a net spin-polarized current by exciting the TSS electrons using circular-polarized light, which can provide an additional contribution to TE transport. For thermal measurements, the  $\mathrm{Bi_2Te_2Se}$  films were suspended on holey SiN membranes, while for electrical measurements, the films were exfoliated onto SiO2/Si substrates followed by fabrication of Au/Cr electrodes. "Nanostructured" films were fabricated by patterning nanostructure arrays of circular holes with depth of  $\sim 3-4$  nm (less than the TI film thickness) and with diameter (D) of 50 nm on the Bi<sub>2</sub>Te<sub>2</sub>Se films via focused ion beam milling using a helium ion microscope (HIM). On the other hand, "pristine" films refer to the as-exfoliated Bi<sub>2</sub>Te<sub>2</sub>Se films, that have not undergone any patterning. A

detailed description of the sample preparation is provided in the Experimental Section.

The thickness-dependent in-plane thermal conductivity k of the suspended Bi<sub>2</sub>Te<sub>2</sub>Se films was measured at room temperature using micro-Raman thermometry and the results are presented in Figure 1c. The detailed measurement procedure is described later in the text. The measured thermal conductivity of the pristine films starts increasing sharply from the bulk value of about 1 W/mK when the thickness is reduced to below ~25 nm, reaching 2.95 W/mK when the thickness is around 10 nm. This measured value is the sum of the individual contributions from the phonons  $k_{\rm ph}$ , the bulk carriers  $k_{e}$ , and the TSS  $k_{TSS}$ , which is consistent with our previous work.<sup>37</sup> The thickness-dependent surface and bulk contributions to the thermal conductivity in pristine Bi<sub>2</sub>Te<sub>2</sub>Se films has been estimated using a simple two-layer transport model and presented in Supporting Note S1. A violation of the Wiedemann-Franz law is observed, and a large value of Lorenz number, more than 9 times the Sommerfeld value  $L_0$ , is also calculated for the thin films, which was also found in our previous work.<sup>37</sup> This is attributed to the increasingly TSSdominated thermal transport in thin pristine films which can also explain the rapid increase in thermal conductivity. On the other hand, the measured thermal conductivity of the nanostructured films decreases with thickness reduction, with the lowest value of 0.31 W/mK attained for a 10 nm film. This film was patterned with a circular hole array of diameter D =50 nm and depth of  $\sim$ 4 nm with nanostructure period P = 100nm. This measured thermal conductivity is lower than experimentally reported values for other TI thin films<sup>39-41</sup> and is also comparable to the thermal conductivity of more complex TI structures like superlattices<sup>31,54</sup> and heterostructures.55 The reduction in thermal conductivity by a factor of ~9.5 for the 10 nm nanostructured film compared with the pristine film of the same thickness is ascribed to a combined reduction in  $k_{\rm ph}$ ,  $k_{\rm e}$  and  $k_{\rm TSS}$ . The suppression in  $k_{\rm ph}$  can be explained by increased phonon scattering from the nanostructure boundaries, as phonons with mean free path (MFP) greater than 50 nm can contribute up to ~30% of the lattice thermal conductivity in  $Bi_2Te_2Se.^{56}$  Similarly,  $k_e$  can also be suppressed due to increased electron scattering. On the other hand, TSS are expected to be robust to the nanostructuring as they are insensitive to spin-independent scattering due to their unique spin-texture.<sup>23</sup> This indicates that the observed reduction in  $k_{TSS}$  must originate from another mechanism. In our earlier work, we demonstrated that the thermal conductivity of Bi<sub>2</sub>Te<sub>2</sub>Se films is very sensitive to the location of the chemical potential relative to the Dirac point.<sup>38</sup> When the chemical potential is close to the Dirac point, thermal transport is dominated by the TSS, leading to a high thermal conductivity. On the other hand, when the chemical potential moves closer to the bulk bands, the contribution from the TSS can be diminished, which results in the phonons and bulk carriers contributing to the majority of the thermal transport and a reduction in total thermal conductivity.

The shift in the chemical potential due to nanostructuring is verified by extracting the carrier concentration of the films through Hall effect measurements using six-terminal Hall bar devices fabricated on  $SiO_2/Si$  substrates. It is important to ensure that the thermal and electrical properties of the  $Bi_2Te_2Se$  films are not altered during the device fabrication or due to the presence of the  $SiO_2/Si$  substrate as compared to the suspended films. This has been verified in our previous

work<sup>37</sup> by first patterning the electrodes on the holey SiN membrane followed by subsequent transfer of the Bi<sub>2</sub>Te<sub>2</sub>Se films directly onto the contacts. This process confirms that the Bi<sub>2</sub>Te<sub>2</sub>Se films do not undergo any device fabrication and that the same films can be used both for thermal and electrical measurements. Based on these findings, the thickness-dependent sheet carrier density  $n_s$  of the pristine and nanostructured films on SiO<sub>2</sub>/Si substrates was measured at room temperature and the results are presented in Figure 1d. The sheet carrier density is obtained from the measured Hall coefficient  $R_{\rm H}$ using a single-band model,  $n = 1/R_{H}e$ . Bi<sub>2</sub>Te<sub>2</sub>Se samples with thickness larger than ~25 nm demonstrate p-type behavior, indicating that the electrical transport in thicker films is dominated by bulk holes. On the other hand, in thinner samples, the Hall coefficient R<sub>H</sub> flips sign, indicating a transition to TSS-dominated electronic transport. The extracted  $n_s$  for the pristine thin films approaches  $\sim 1 \times 10^{13}$ cm<sup>-2</sup>, which is lower than the carrier concentration when the chemical potential is located at the bottom of the conduction band, as measured by previous ARPES measurements to be  $\sim$ 2  $\times$  10<sup>13</sup> cm<sup>-253</sup>. This indicates that the chemical potential in the pristine films is indeed closer to the Dirac point, which aligns with its high measured thermal conductivity. After nanostructuring, the measured  $n_s$  of the films is significantly higher, indicating that the chemical potential has shifted toward the conduction band, which reduces the contribution of the TSS to thermal transport and leads to lower thermal conductivity. The inset of Figure 1d. illustrates the location of the chemical potential relative to the bulk bands and the TSS in films of different thickness. More details of the Hall effect measurements are provided in Supporting Note S2. A possible reason for the increase in carrier concentration in the nanostructured film is due to the creation of donor-like point defects during the He<sup>+</sup> ion beam irradiation. The formation of such defects due to ion-beam irradiation has been experimentally observed in similar materials such as Bi<sub>2</sub>Te<sub>3</sub>, 46,57 along with other 2D materials. 58,59 Such defects have been found to enhance the TE properties of the material as they can act as electron donors, which can increase the chemical potential while simultaneously acting as electron and phonon scattering centers, which reduces the thermal conductivity. In the case of Bi<sub>2</sub>Te<sub>2</sub>Se, the He<sup>+</sup> ion beam is likely to generate Se/Te vacancies, which can act as n-type dopants. Hence, the suppressed thermal conductivity measured in the nanostructured Bi<sub>2</sub>Te<sub>2</sub>Se films is due to the combined effects of increased electron and phonon scattering along with the reduction of TSS contribution to the thermal transport.

The sheet resistance  $R_S$  of the  $Bi_2Te_2Se$  films was measured using a standard four-probe technique and used to calculate the electrical conductivity  $\sigma$ . A detailed description of the measurements is provided in the Experimental Section. The calculated thickness-dependent electrical conductivity  $\sigma$  of the pristine and nanostructured films is presented in Figure 1e. The measured electrical conductivity of the pristine films also increases rapidly when the thickness is below ~25 nm due to increased TSS contribution to the transport, similar to the trend observed for thermal conductivity in Figure 1c. However, a crucial finding for improving TE performance is that the electrical conductivity of thinner nanostructured films does not deteriorate as significantly as the thermal conductivity. It is also seen from Figure 1c,e that the alteration of transport properties of the Bi<sub>2</sub>Te<sub>2</sub>Se films due to the effects of nanostructuring is less prominent with increasing film thickness. This is because

since the same He<sup>+</sup> ion dose was used to pattern the nanostructures, the depth of the structures across all samples is similar, estimated to be only a few nm. A nanostructure that is a few nm deep is expected to impede TE transport significantly in thinner films due to increased surface scattering, while in thicker films, most of the phonon and electron transport in the bulk remains largely unaffected.

Potential damage or residue deposition on the surface of the Bi<sub>2</sub>Te<sub>2</sub>Se films during the nanostructuring is also a great concern. To ensure that the exposure to the He+ ion beam does not significantly damage the material structure and impair the surface states, we conduct thorough investigations and demonstrate the presence of the circular photogalvanic effect (CPGE) and the weak antilocalization (WAL) effect in our nanostructured films. The generation of a net spin-polarized current from thin Bi<sub>2</sub>Te<sub>2</sub>Se films using circularly polarized light is illustrated in Figure 1b. This type of optical response to circularly polarized light is called CPGE which has been widely discussed and has also been demonstrated in our previous work. 50,61,62 In the case of TI, this response arises exclusively from the TSS and not from the bulk due to the coupling of the spin of the surface states with the incident photons. 43,63 In our experiments, a 632.8 nm He Ne laser was focused on the center of a Bi<sub>2</sub>Te<sub>2</sub>Se device, obliquely incident at an angle of 45°. The incident laser polarization is altered using a quarterwave plate (QWP). A detailed description of the photocurrent measurements is provided later in the text and the Experimental Section. The measured polarization-dependent photocurrent as a function of QWP angle  $(\phi)$  is presented in Figure 1f. The experiments were performed on the same 10 nm thick Bi<sub>2</sub>Te<sub>2</sub>Se device before and after fabricating the nanostructures. The total measured polarization-dependent photocurrent includes additional components generated from other mechanisms along with the desired CPGE, and can be described by eq 1<sup>43</sup>

$$I = D + C\sin(2\phi) + L_1\sin(4\phi) + L_2\cos(4\phi)$$
 (1)

where the C term is associated with the desired circular photoresponse,  $L_1$  and  $L_2$  terms depend on the linear polarization of light, and the D term originates from the photothermoelectric background arising from the bulk and is polarization insensitive. The measured polarization-dependent data was fit using eq 1, and the results are presented as the dashed lines in Figure 1f. From the fitting results, a dominating CPGE contribution to the total photocurrent is apparent for both the pristine and nanostructured film, along with a trend that distinctly follows a 180° period, as observed in Figure 1f. The obtained circular photoresponse term C from the fitting are 1.647 nA and 0.775 nA for the pristine and nanostructured film, respectively. The presence of such a strong polarizationdependent photocurrent indicates that the TSS has not been damaged during the nanostructuring. Such a robust nature of the surface states has also been theoretically predicted and experimentally observed earlier in thin TI films. 33,57,64 In addition to CPGE, low-temperature magnetotransport measurements were also performed on thin Bi<sub>2</sub>Te<sub>2</sub>Se films and the results are presented in Supporting Note S2. The presence of the WAL effect was observed in a 9 nm thick device before and after the nanostructuring, providing additional evidence of the robust nature of the TSS. The retention of TSS properties like their unique spin-orbit coupling also enables the use of the nanostructured Bi<sub>2</sub>Te<sub>2</sub>Se films in variety of on-chip photonic

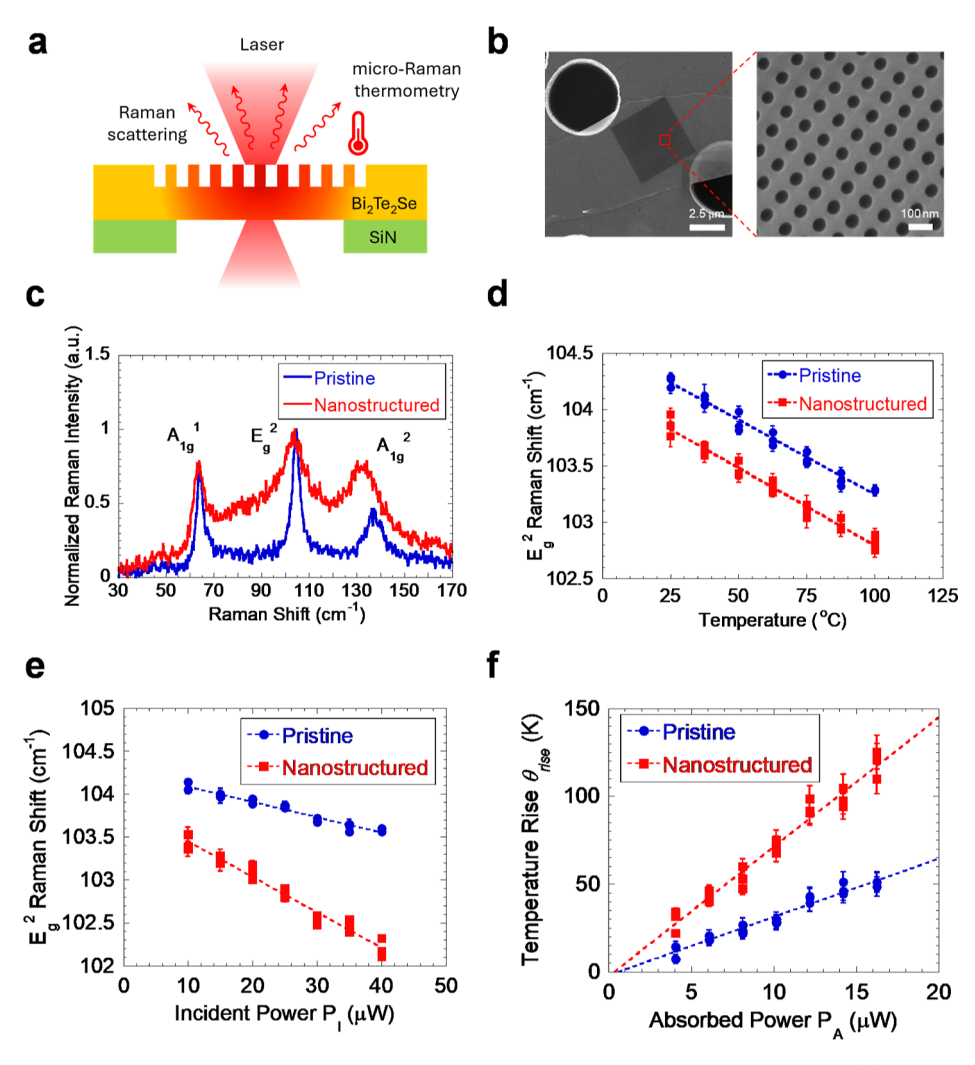


Figure 2. Preparation and micro-Raman thermometry of suspended pristine and nanostructured  $Bi_2Te_2Se$  films. (a) Schematic representation of a 632.8 nm laser focused on the center of a nanostructured  $Bi_2Te_2Se$  film suspended on a holey SiN membrane for thermal conductivity measurements. (b) Helium ion microscope image of a suspended nanostructured  $Bi_2Te_2Se$  film. (c) Raman spectra of a suspended 10 nm thick  $Bi_2Te_2Se$  film collected before and after fabricating the nanostructures.  $E_g^2$  Raman peak shift of the samples as a function of (d) temperature and (e) incident laser power  $P_I$ . (f) Calculated temperature rise  $\theta_{rise}$  in both samples as a function of absorbed laser power  $P_A$ . Dashed lines indicate linear fits to the data.

applications like chirality detection, as demonstrated in our previous work.  $^{50}$ 

The in-plane thermal conductivity of Bi<sub>2</sub>Te<sub>2</sub>Se films is measured using micro-Raman thermometry, a technique that is adapted from our previous work, 35-38 as illustrated in Figure 2a. Briefly, micro-Raman thermometry is a noncontact optical technique used to measure the in-plane thermal conductivity of thin films. In this method, a focused laser beam simultaneously acts as a localized heat source and an excitation source for Raman scattering on a suspended thin film. The local heating induced by the laser causes a temperature rise in the film, which leads to a measurable redshift in specific Raman phonon modes. By collecting Raman spectra at varying laser powers and temperatures, the shift in Raman peak position is calibrated as an optical thermometer, enabling the correlation between laser-induced temperature rise and absorbed power. The absorbed laser power is determined by measuring the film's reflectivity and transmissivity at the laser wavelength. A detailed steady-state three-dimensional heat conduction model incorporating the laser spot size, film thickness, and optical penetration depth is then used to simulate the temperature rise

in the suspended film. Matching the experimentally measured temperature rise with the model predictions yields the in-plane thermal conductivity of the thin film with high sensitivity and accuracy. Figure 2a also shows that it is preferable to suspend the films during the in-plane thermal conductivity measurement, so that the contribution to the thermal transport by the substrate can be removed and the sensitivity of the measurement can be preserved. A more detailed description of the micro-Raman thermometry measurements and numerical modeling is provided in Supporting Note S3. HIM images of a nanostructured suspended Bi<sub>2</sub>Te<sub>2</sub>Se film are presented in Figure 2b. The Raman spectra of a 10 nm thick suspended film collected before and after fabricating the nanostructures is shown in Figure 2c. It is observed that there is a slight shift in the locations of the Raman peaks, along with a significant broadening of the peak widths after the nanostructuring. A possible reason for the peak shift could be the change in carrier concentration due to the He+ ion patterning, as observed previously in other 2D materials. The peak broadening can be associated with a possible decrease in the phonon lifetime due to increased scattering events in the nanostructured film, which

**ACS Applied Materials & Interfaces** 

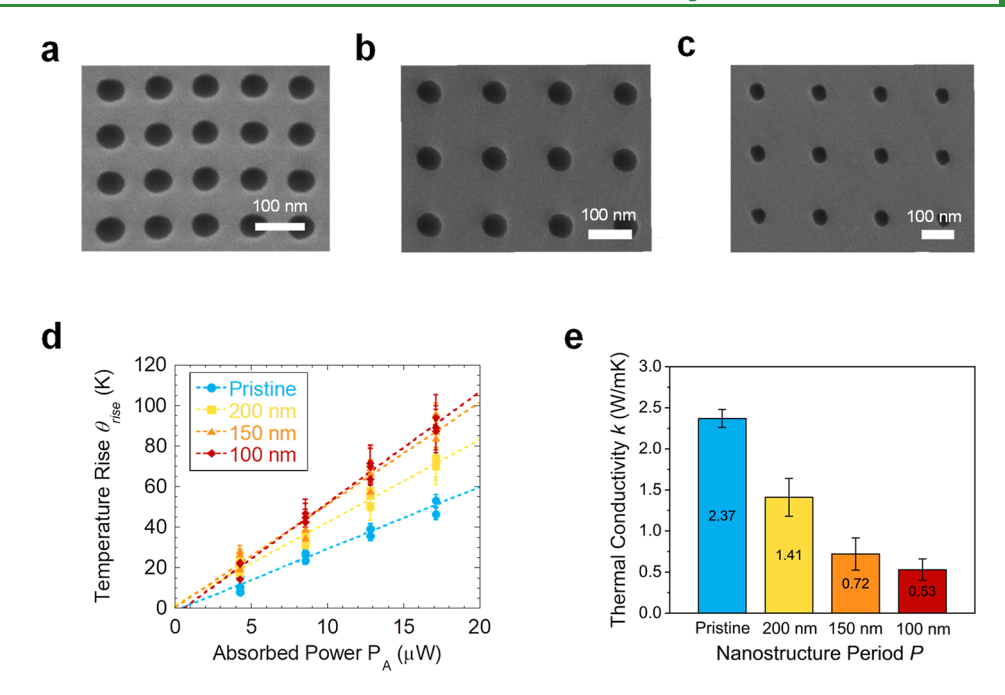


Figure 3. Effect of nanostructure period on measured in-plane thermal conductivity. Helium ion microscope images of circular hole array of diameter D = 50 nm patterned on Bi<sub>2</sub>Te<sub>2</sub>Se films with varying period P of (a) 100 nm, (b) 150 nm and (c) 200 nm. All scale bars have length 100 nm. (d) Temperature rise  $\theta_{\text{rise}}$  of multiple 16 nm thick Bi<sub>2</sub>Te<sub>2</sub>Se films with different nanostructure period P as a function of absorbed laser power  $P_A$ . Dashed lines are linear fits to the data. (e) Extracted in-plane thermal conductivities of the pristine and nanostructured samples using the fitting.

also aligns with the reduction in its measured in-plane thermal conductivity. A similar red shift and broadening of the Raman peaks after He<sup>+</sup> ion irradiation has also been reported in a similar material  $Bi_2Te_3$ . The  $E_g^2$  mode of the Raman spectrum is used as the optical thermometer in our measurements due to its high sensitivity to temperature change. The change in the location of the  $E_{\rm g}^{'2}$  peak of both the pristine and nanostructured film as a function of temperature and incident A power P<sub>I</sub> are presented in Figure 2d,e, respectively. The data shows a linear trend with both the temperature and laser power, similar to previous Raman thermometry measurements. The results of the linear fitting are represented as dashed lines, and their slopes are used to extract the first-order temperature coefficient  $\chi_T = \Delta \omega / \Delta T$  and the first-order power coefficient  $\chi_P = \Delta \omega / \Delta P_{\rm I}$ , respectively, where  $\Delta \omega$  is the frequency shift. It is observed that  $\chi_T$  remains nearly the same after nanostructuring. However, there is a significant increase in magnitude in  $\chi_P$ , which indicates a reduction in the in-plane thermal conductivity. The optical properties of the suspended films were then measured (see Experimental Section and Supporting Note S4 for more details) and used to compute the temperature rise  $\theta_{\rm rise}$  as a function of absorbed power  $P_A$  as presented in Figure 2f. The measured optical properties of the Bi<sub>2</sub>Te<sub>2</sub>Se films do not change significantly after the nanostructuring. Rigorous coupled-wave analysis (RCWA) calculations are also performed to rule out the possibility of strong optical interference from the periodic array. The optical properties obtained from the RCWA calculations match well with the experimentally measured values and are presented in Supporting Note S4. The in-plane thermal conductivity k of the films is finally extracted by matching the measured temperature rise per unit absorbed power to a three-dimensional numerical heat conduction model. This yields a thermal conductivity of 0.31  $\pm$  0.10 W/ mK and  $2.95 \pm 0.31$  W/mK for the 10 nm thick

nanostructured and pristine film, respectively. Note that the reported thermal conductivity of the Bi<sub>2</sub>Te<sub>2</sub>Se films is an average value over the temperature calibration range. A detailed discussion on the uncertainties during the thermal conductivity measurements has been provided in Supporting Note S5.

To further study the suppression of thermal transport due to increased scattering from the nanostructures, we perform thermal conductivity measurements on suspended Bi<sub>2</sub>Te<sub>2</sub>Se films patterned with different nanostructure arrays. HIM images of different circular hole arrays of diameter D = 50nm with varying periods P of 100, 150, and 200 nm are presented in Figure 3a-c. The thermal conductivity measurements were performed on two different films of similar thickness ~16 nm, with arrays of varying periods. The measured temperature rise  $\theta_{\mathrm{rise}}$  in films as a function of absorbed power  $P_A$  is presented in Figure 3d. The temperature rise per unit absorbed power in the films is observed to increase monotonically with reduced spacing between the nanostructures, which indicates a stronger suppression in thermal transport. This trend of reduction in thermal conductivity with reduction in the array spacing has been well-studied theoretically and also experimentally observed in other periodic nanostructures. The final extracted in-plane thermal conductivity of the films is presented in Figure 3e, which shows a ~78% reduction in thermal conductivity from 2.37 W/mK in the pristine film to 0.53 W/mK in the nanostructured film with period 100 nm. As discussed earlier in the text, such a drastic suppression in the measured total thermal conductivityis likely to arise from a combined reduction in  $k_{TSS}$  along with  $k_{ph}$  and  $k_{e}$ . The reduction in  $k_{ph}$ arises from the fact that the surface of the nanostructures can effectively scatter phonons with mean free path (MFP) that are comparable or greater than the spacing between them. This observed reduction in  $k_{\rm ph}$  also aligns with recent theoretical

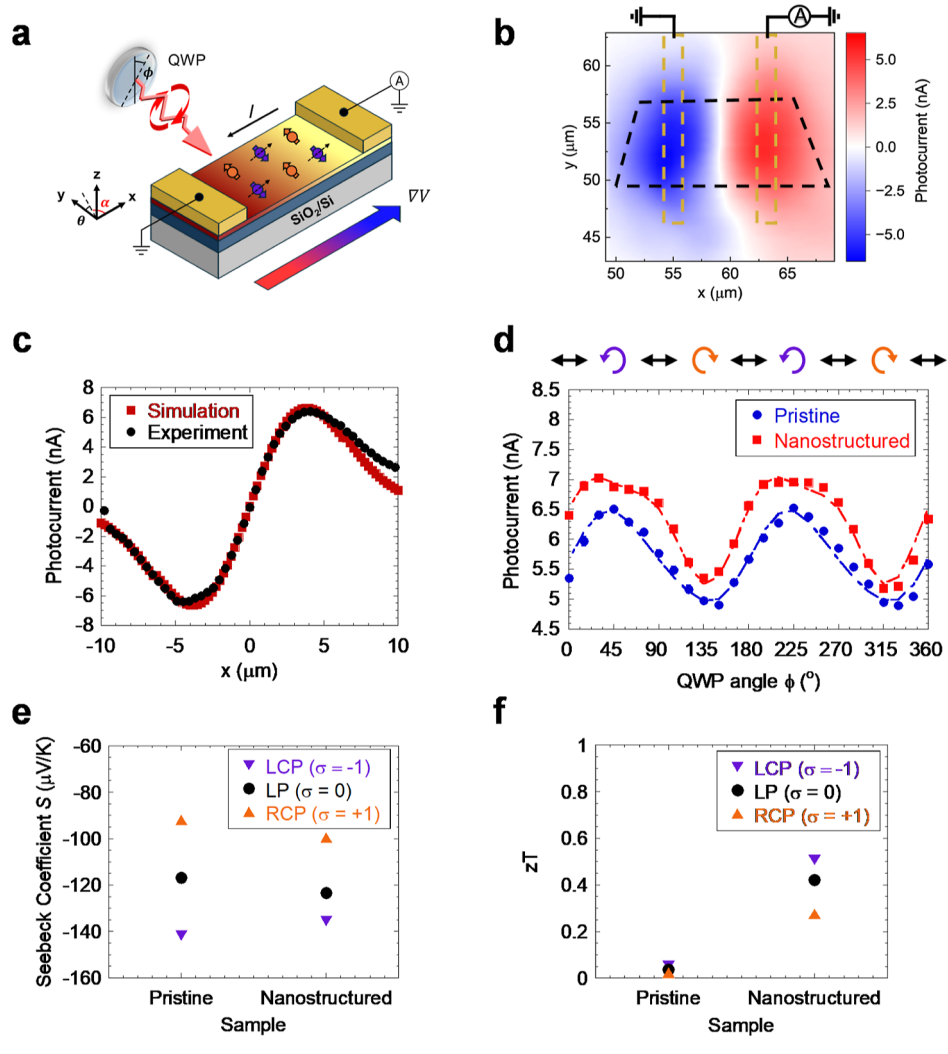


Figure 4. Seebeck coefficient extraction of pristine and nanostructured  $Bi_2Te_2Se$  films with optical spin injection. (a) Schematic of the photocurrent measurement setup with a 632.8 nm laser incident at angle  $\theta=45^{\circ}$  focused on the device. The polarization of the incident light can be varied by using a quarter wave plate. (b) Photocurrent mapping of a 10 nm thick nanostructured  $Bi_2Te_2Se$  device under linear polarized (LP) light. (c) Measured short-circuit photocurrent when the LP laser spot is scanned along the center of the device channel. The red curve indicates the short-circuit photocurrent profile along the channel obtained by using the best fit Seebeck coefficient from the numerical simulation. (d) Measured photocurrent as a function of incident light polarization when the laser spot is focused on the one of the device contacts. An increased (decreased) net photocurrent is observed due to optical spin injection under left (right) circularly polarized light. (e) The extracted value of helicity-tuned Seebeck coefficient from the model under optical spin injection. (f) The thermoelectric figure of merit zT calculated using the measured thermoelectric properties. The calculated zT of the nanostructured film is  $\sim$ 0.42 under linear polarized light (more than 11 times higher than the pristine film) which can be further improved to  $\sim$ 0.50 under optical spin injection.

studies on  $\mathrm{Bi_2Te_2Se}$ , which have suggested that phonons having MFP >50 nm can contribute to ~30% of lattice thermal conductivity at room temperature. Thermal conductivity measurements performed on another 21 nm thick  $\mathrm{Bi_2Te_2Se}$  film with different nanostructure periods has been provided in Supporting Note S6.

Lastly, we study the Seebeck coefficients of the nanostructured films. A schematic of the experimental setup to extract the Seebeck coefficient of the  ${\rm Bi_2Te_2Se}$  films is presented in Figure 4a. In our experiments, a 632.8 nm He Ne laser is focused to a spot size of ~5  $\mu$ m onto  ${\rm Bi_2Te_2Se}$  devices at an oblique incident angle  $\theta$  of 45° with the x-y plane. The angle of the incident beam with the x-axis is defined as  $\alpha$  and kept as 90° in our measurements. Since, in  ${\rm Bi_2Te_2Se}$ , the spin-polarization of the TSS is locked perpendicular to its momentum, <sup>66</sup> this orientation of laser incidence allows the coupling between circularly polarized light and the electron

spins of the TSS to generate a measurable net spin-polarized current along the device channel, 43 as illustrated in Figure 4a. The polarization of the incoming laser is controlled by rotating a QWP by an angle  $\phi$  which can convert linear polarized (LP,  $\phi = 0^{\circ}$ ) light into left circularly polarized (LCP,  $\phi = 45^{\circ}$ ) or right circularly polarized (RCP,  $\phi = 135^{\circ}$ ) light. Figure 4a also illustrates that the laser spot locally heats the Bi<sub>2</sub>Te<sub>2</sub>Se film and creates a temperature gradient across the device, which drives the generated carriers and leads to a measurable short-circuit photocurrent. The photocurrent of all the devices in our experiments is measured at room temperature with zero source-drain and gate bias ( $V_{\rm DS}$  = 0 V, $V_{\rm G}$  = 0 V). The shortcircuit photocurrent of a 10 nm thick nanostructured film is measured under LP light as the laser spot is scanned over the device, and the resulting photocurrent map is shown in Figure 4b. The dashed gold and black lines in the figure indicate the geometry of the Au contacts and the Bi<sub>2</sub>Te<sub>2</sub>Se film,

respectively. The polarity of the dominant charge carriers is determined as n-type based on the photocurrent pattern, which aligns with our earlier described Hall measurements. The center of the channel can be found as the location where the photothermoelectric current is minimum.

To extract the Seebeck coefficient of the Bi<sub>2</sub>Te<sub>2</sub>Se film, a numerical photothermoelectric model is solved, which couples the temperature rise in the film due to laser heating with the measured short-circuit photocurrent. The thermal, optical, and electrical properties of the film, which were measured using the approaches described earlier in the text, are used as inputs to the model to obtain a value of Seebeck coefficient that best fits the measured short-circuit photocurrent from our experiments. The numerical model is adapted from our previous work, 61 where this approach for extracting Seebeck coefficient was validated against experiments by directly measuring the developed Seebeck voltage as a function of the temperature rise in the film using micro-Raman thermometry. A detailed description of the photothermoelectric model is provided in Supporting Note S7. The profile of the experimentally measured short-circuit photocurrent in the 10 nm thick nanostructured film under LP light as the laser spot is scanned along the length of the device channel is presented in Figure 4c, along with the results of the numerical simulation. The extracted value of Seebeck coefficient for the nanostructured film is  $-123.43 \,\mu\text{V/K}$ , while it was found to be  $-116.95 \,\mu\text{V/K}$ before the nanostructuring. These obtained values include the contributions from both the TSS and the bulk states and are sensitive to the location of the chemical potential.<sup>26</sup> The Seebeck coefficient extraction for a thicker Bi<sub>2</sub>Te<sub>2</sub>Se device, which demonstrates p-type behavior, is provided in Supporting Note S8. The obtained Seebeck coefficients match well with reported values from other TI films where the Seebeck coefficient of the bulk states with parabolic band dispersion is usually higher in magnitude than the TSS with linear dispersion. 27,61 In addition to the photothermoelectric current, we use LCP(RCP) light to selectively excite down(up) spin electrons of the TSS to generate a net spin-polarized current, which is aligned along(against) the carrier flow driven by the temperature gradient in the device. The polarization-dependent short-circuit photocurrent generated when the laser spot is focused near one of the contacts of the device, is presented in Figure 4d. This measurement is also performed on the same 10 nm thick device before and after the nanostructures are patterned. The dashed lines in the figure indicate the obtained results of the fitting of the polarization-dependent photocurrent using eq 1. It is found that a larger short-circuit photocurrent is obtained under LCP light. The apparent Seebeck coefficient in the pristine and nanostructured films under LCP light are found to be  $-141.76 \mu V/K$  and -135.38 $\mu V/K$ , respectively. Correspondingly, a similar enhancement in the short-circuit photocurrent and Seebeck coefficient is observed under RCP light when the laser spot is focused on the other contact of the device. The comparison between the polarization-dependent short-circuit photocurrent obtained when the laser beam is focused on different contacts of the 10 nm thick nanostructured device is discussed in Supporting Note S7. The further enhancement of Seebeck coefficient in the Bi<sub>2</sub>Te<sub>2</sub>Se films is challenging as the Seebeck coefficient of the TSS is inherently limited to a maximum value of  $\sim -160$  $\mu V/K$  as shown in our earlier work using the Landauer formalism.<sup>61</sup> Figure 4e shows the values of the helicity-tuned Seebeck coefficient under optical spin injection for both the

pristine and nanostructured film. A slightly higher magnitude of Seebeck coefficient obtained under LP light for the nanostructured film indicates that bulk electrons now play a more important role in TE transport as compared to the pristine film. On the other hand, a slightly higher fraction of CPGE to the bulk photocurrent (C/D ratio) is obtained in the pristine film, and it is found that its Seebeck coefficient can be tuned much more effectively under optical spin injection. This suggests that the chemical potential in the pristine film is closer to the Dirac point as the electrical and optical responses from the TSS become more prominent when the chemical potential is near the middle of the bulk bandgap due to reduced scattering of the TSS with the bulk states.<sup>67</sup> Both of the above observations indicate that the chemical potential in Bi<sub>2</sub>Te<sub>2</sub>Se films shifts toward the conduction band due to nanostructuring, which also aligns with our obtained thermal conductivity and Hall measurement results.

Finally, after obtaining all the crucial TE parameters, the figure-of-merit  $zT = S^2 \sigma T/k$  and power factor PF =  $S^2 \sigma$  was calculated for both the pristine and nanostructured film under optical spin injection, and the results are presented in Figure 4f. It is found that the calculated PF for the nanostructured film is 435.71  $\mu$ W/mK<sup>2</sup> and zT is ~0.42 under LP light, a value that is more than 11 times higher than the pristine film at room temperature. The drastic increase in zT mainly stems from the highly suppressed thermal conductivity in the nanostructured film, along with a slight improvement in the Seebeck coefficient. The enhanced apparent Seebeck coefficient obtained for the 10 nm thick nanostructured film using optical spin injection can lead to a further improvement in zT to  $\sim$ 0.50 and PF to 524.17  $\mu$ W/mK<sup>2</sup> under LCP light. The obtained value for PF in our Bi<sub>2</sub>Te<sub>2</sub>Se system is comparable to and the value of zT in our Bi<sub>2</sub>Te<sub>2</sub>Se system is higher than reported values for other thin film TIs. 40,45,46,70 However, the further enhancement of TE properties is limited by the inherent low value of the Seebeck coefficient of the TSS in TI films.

# CONCLUSIONS

In summary, in this work we present experimental studies of TE properties in thin TI films Bi<sub>2</sub>Te<sub>2</sub>Se. We demonstrate that nanostructuring can be used as an effective approach to drastically suppress thermal conductivity in Bi<sub>2</sub>Te<sub>2</sub>Se without causing a significant deterioration in electrical conductivity or Seebeck coefficient, while retaining the unique properties of the TSS. The thermal conductivity of a 10 nm thick nanostructured film was measured to be 0.31 W/mK at room temperature, a value which is nearly an order of magnitude lower than a pristine film of the same thickness, and is close to the amorphous limit. Moreover, we obtain a greatly enhanced zT of 0.42 in the nanostructured film, a factor  $\sim$ 11 times larger than the pristine film. The unique spin texture of the TSS of Bi<sub>2</sub>Te<sub>2</sub>Se also allows the generation of an additional spin-polarized current parallel to the current driven by the temperature gradient, which results in an enhanced apparent Seebeck coefficient and a further improved zT of 0.50 at room temperature—a value which is higher than those reported for most thin film TIs. We also investigate how the relative contribution of the TSS and the bulk states affect the TE transport across multiple Bi<sub>2</sub>Te<sub>2</sub>Se films with varying thickness. Our results demonstrate the potential for tuning TE properties in thin film TIs through nanostructuring and making our Bi<sub>2</sub>Te<sub>2</sub>Se itself as a cooling device, and hence, an alternative to

more complex structures and materials. TE devices made of such thin film TIs, which can also be optically modulated, can be promising candidates for compact solid-state cooling solutions for nanoscale electronic and spintronic devices.

#### **■ EXPERIMENTAL SECTION**

**Sample Preparation.** For thermal measurements, Bi<sub>2</sub>Te<sub>2</sub>Se flakes were exfoliated using Nitto dicing tapes from bulk crystals grown by the Bridgeman method<sup>53</sup> and then released onto a poly(methyl methacrylate) (PMMA, 950 A4) and poly(vinyl alcohol) (PVA) thin film stack spin-coated on a Si wafer. The film stack was examined under an optical microscope to identify candidate flakes for transfer based on the optical contrast, with thickness later confirmed by atomic force microscopy (AFM, AIST-NT). The desired flakes were then precisely aligned to holey silicon nitride membranes (Ted Pella) and attached. The whole sample was then dipped into acetone to dissolve the PMMA, leaving the Bi<sub>2</sub>Te<sub>2</sub>Se flakes suspended on the holes for micro-Raman thermometry measurements. For electrical measurements, the Bi<sub>2</sub>Te<sub>2</sub>Se flakes were exfoliated onto heavily doped Si substrates capped with 90 nm SiO<sub>2</sub>. Candidate flakes were selected under the optical microscope and characterized using AFM. The devices were fabricated by electron beam lithography followed by the deposition of Au/Cr (90 nm/5 nm) contacts using electron beam evaporation. We refer to the as-exfoliated Bi<sub>2</sub>Te<sub>2</sub>Se films, that have not undergone any patterning as "pristine". After preparing the suspended films and electrical devices, nanostructures were finally patterned onto them using a Zeiss Orion NanoFab helium ion microscope (HIM), creating the "nanostructured" films. An accelerating voltage of 25 keV was used for all exposures with a  $\mathrm{He^{+}}$  ion dose of  $\sim 4 \times 10^{17}$  ions/cm<sup>2</sup>. Arrays of circular holes with 50 nm diameter were patterned on the samples with varying periods of 100, 150, and 200 nm. The prepared samples were stored under vacuum in between measurements.

Micro-Raman Thermometry and Optical Property Measurements. Raman thermometry and optical property measurements were performed on suspended Bi<sub>2</sub>Te<sub>2</sub>Se films (without the substrate). A HORIBA LabRAM HR800 Raman spectrometer equipped with a 632.8 nm wavelength He-Ne laser was used for all Raman measurements. The laser was focused on the suspended Bi<sub>2</sub>Te<sub>2</sub>Se films using a 100× objective (Olympus MPlan, N.A. = 0.90) to a spot size of  $\sim$ 0.48  $\mu$ m, acting both as a steady-state heat source and Raman excitation source. The acquired Raman spectra were fitted using a Lorentzian function to extract the Raman peak positions. The grating used has a groove density of 1800 L/mm, which gives a nominal spectral resolution of 0.27 cm<sup>-1</sup> per pixel. The Lorentzian peak fitting yields a peak position shift uncertainty of less than 0.02 cm corresponding to a temperature rise measurement uncertainty of less than 1 K. The reflectivity and transmissivity of each suspended film were measured by the same laser using a power meter (Newport 1815 C). The amount of absorbed laser power was derived from the reflectivity, transmissivity, and total incident laser power and was subsequently used as heat source input for the numerical heat transfer model to extract the in-plane thermal conductivity of the suspended thin film. The measured thickness-dependent optical properties of the suspended films were fit to an optical model to extract the refractive index of Bi<sub>2</sub>Te<sub>2</sub>Se at 632.8 nm. More details can be found in Supporting Notes S3 and S4.

**Electrical Transport Measurements.** Hall effect measurements were performed on six-terminal Hall bar devices on  $SiO_2/Si$  substrates inside a Lakeshore CRX-VF cryogenic probe station, which allows a temperature range from 10 to 420 K and an applied magnetic field up to  $\pm 2.5$  T. The transverse Hall resistance  $R_{xy}$  signal was antisymmetrized to correct the geometry effects and misalignment of the contacts. The sample resistances were measured by a four-probe method using a Stanford Research SR830 lock-in amplifier with a low frequency ( $\sim 17.7$  Hz) excitation current of 1 μA from a Keithley 6221 source meter. The sheet resistance of the devices was calculated from the longitudinal resistance  $R_S = R_{xx} \times W/L$ , where W

and L are the width and length of the conduction channel in the device, respectively.

Photocurrent Measurements and Seebeck Coefficient Extraction. A 632.8 nm wavelength He—Ne laser was focused using a longworking distance objective (Mitutoyo  $10\times$  M Plan Apo, N.A. = 0.28) to a spot size of  $\sim$ 5  $\mu$ m and an incident angle of 45°. The laser spot was scanned along the channel of Bi<sub>2</sub>Te<sub>2</sub>Se devices on SiO<sub>2</sub>/Si substrates using a piezoelectric nanopositioner. A quarter-wave plate (QWP) was used to control the polarization of the beam and convert it from linearly polarized to left/right circular polarized. The photocurrent was measured using a DC source meter (Keithley 2612A). The measured short-circuit photocurrent was used as an input for a numerical photothermoelectric model, which is used to extract the Seebeck coefficient from the temperature rise in the device due to laser heating. More details can be found in Supporting Notes S7 and S8. All measurements were performed at zero source-drain bias and zero gate bias at room temperature.

## ASSOCIATED CONTENT

# **Solution** Supporting Information

The Supporting Information is available free of charge at https://pubs.acs.org/doi/10.1021/acsami.5c14518.

Large surface Lorenz number of pristine  $Bi_2Te_2Se$  films and extracted bulk thermal and electrical conductivities, Hall effect measurements of pristine and nanostructured  $Bi_2Te_2Se$  films, micro-Raman thermometry measurements, thickness-dependent optical property measurements of  $Bi_2Te_2Se$  films at 632.8 nm, uncertainty analysis in thermal conductivity measurement, nanostructure period effect on thermal conductivity, numerical simulation for extracting thermoelectric properties, and hole dominated transport in thick  $Bi_2Te_2Se$  films (PDF)

#### AUTHOR INFORMATION

## **Corresponding Author**

Xianfan Xu — School of Mechanical Engineering, Purdue University, West Lafayette, Indiana 47907, United States; Birck Nanotechnology Center and Elmore Family School of Electrical and Computer Engineering, Purdue University, West Lafayette, Indiana 47907, United States; ◎ orcid.org/ 0000-0003-0580-4625; Email: xxu@ecn.purdue.edu

## **Authors**

Neil Ghosh — School of Mechanical Engineering, Purdue University, West Lafayette, Indiana 47907, United States; Birck Nanotechnology Center, Purdue University, West Lafayette, Indiana 47907, United States; orcid.org/0000-0002-0527-011X

Yong P. Chen — Birck Nanotechnology Center, Elmore Family School of Electrical and Computer Engineering, Department of Physics and Astronomy, and Purdue Quantum Science and Engineering Institute, Purdue University, West Lafayette, Indiana 47907, United States

Complete contact information is available at: https://pubs.acs.org/10.1021/acsami.5c14518

## **Author Contributions**

X.X. conceived the idea and supervised the project. N.G. designed and performed the experiments. All authors cowrote the manuscript.

#### Notes

ı

The authors declare no competing financial interest.

#### ACKNOWLEDGMENTS

Support for this work by the National Science Foundation (CBET-2051525) is gratefully acknowledged. N.G. acknowledges training and support from Dmitry Zemlyanov during Helium ion beam milling, Yikang Chen for performing the RCWA calculations and valuable discussions with Chang Niu and Junwoo Jang on experimental design.

#### REFERENCES

- (1) Bell, L. E. Cooling, Heating, Generating Power, and Recovering Waste Heat with Thermoelectric Systems. *Science* **2008**, *321* (5895), 1457–1461.
- (2) DiSalvo, F. J. Thermoelectric Cooling and Power Generation. *Science* **1999**, 285 (5428), 703–706.
- (3) Snyder, G. J.; Toberer, E. S. Complex Thermoelectric Materials. *Nat. Mater.* **2008**, 7 (2), 105–114.
- (4) Zhao, L.-D.; Lo, S.-H.; Zhang, Y.; Sun, H.; Tan, G.; Uher, C.; Wolverton, C.; Dravid, V. P.; Kanatzidis, M. G. Ultralow Thermal Conductivity and High Thermoelectric Figure of Merit in SnSe Crystals. *Nature* **2014**, *508* (7496), 373–377.
- (5) Liu, H.; Shi, X.; Xu, F.; Zhang, L.; Zhang, W.; Chen, L.; Li, Q.; Uher, C.; Day, T.; Snyder, G. J. Copper Ion Liquid-like Thermoelectrics. *Nat. Mater.* **2012**, *11* (5), 422–425.
- (6) Sales, B. C.; Mandrus, D.; Williams, R. K. Filled Skutterudite Antimonides: A New Class of Thermoelectric Materials. *Science* **1996**, 272 (5266), 1325–1328.
- (7) Zhang, Q.; Song, Q.; Wang, X.; Sun, J.; Zhu, Q.; Dahal, K.; Lin, X.; Cao, F.; Zhou, J.; Chen, S.; Chen, G.; Mao, J.; Ren, Z. Deep Defect Level Engineering: A Strategy of Optimizing the Carrier Concentration for High Thermoelectric Performance. *Energy Environ. Sci.* 2018, 11 (4), 933–940.
- (8) Pei, Y.; LaLonde, A. D.; Heinz, N. A.; Shi, X.; Iwanaga, S.; Wang, H.; Chen, L.; Snyder, G. J. Stabilizing the Optimal Carrier Concentration for High Thermoelectric Efficiency. *Adv. Mater.* **2011**, 23 (47), 5674–5678.
- (9) Pei, Y.; LaLonde, A. D.; Wang, H.; Snyder, G. J. Low Effective Mass Leading to High Thermoelectric Performance. *Energy Environ. Sci.* **2012**, *5* (7), 7963–7969.
- (10) Pei, Y.; Shi, X.; LaLonde, A.; Wang, H.; Chen, L.; Snyder, G. J. Convergence of Electronic Bands for High Performance Bulk Thermoelectrics. *Nature* **2011**, *473* (7345), 66–69.
- (11) Heremans, J. P.; Jovovic, V.; Toberer, E. S.; Saramat, A.; Kurosaki, K.; Charoenphakdee, A.; Yamanaka, S.; Snyder, G. J. Enhancement of Thermoelectric Efficiency in PbTe by Distortion of the Electronic Density of States. *Science* **2008**, 321 (5888), 554–557.
- (12) Lee, M.-J.; Ahn, J.-H.; Sung, J. H.; Heo, H.; Jeon, S. G.; Lee, W.; Song, J. Y.; Hong, K.-H.; Choi, B.; Lee, S.-H.; Jo, M.-H. Thermoelectric Materials by Using Two-Dimensional Materials with Negative Correlation between Electrical and Thermal Conductivity. *Nat. Commun.* **2016**, *7* (1), 12011.
- (13) Pichanusakorn, P.; Bandaru, P. Nanostructured Thermoelectrics. *Materials Science and Engineering: R: Reports* **2010**, *67* (2–4), 19–63.
- (14) Li, J.-F.; Liu, W.-S.; Zhao, L.-D.; Zhou, M. High-Performance Nanostructured Thermoelectric Materials. *NPG Asia Mater.* **2010**, 2 (4), 152–158.
- (15) Hicks, L. D.; Dresselhaus, M. S. Thermoelectric Figure of Merit of a One-Dimensional Conductor. *Phys. Rev. B* **1993**, 47 (24), 16631–16634.
- (16) Hicks, L. D.; Dresselhaus, M. S. Effect of Quantum-Well Structures on the Thermoelectric Figure of Merit. *Phys. Rev. B* **1993**, 47 (19), 12727–12731.
- (17) Biswas, K.; He, J.; Blum, I. D.; Wu, C.-I.; Hogan, T. P.; Seidman, D. N.; Dravid, V. P.; Kanatzidis, M. G. High-Performance Bulk Thermoelectrics with All-Scale Hierarchical Architectures. *Nature* **2012**, *489* (7416), 414–418.

- (18) Kim, W. Strategies for Engineering Phonon Transport in Thermoelectrics. J. Mater. Chem. C Mater. 2015, 3 (40), 10336–10348
- (19) Liu, T. H.; Zhou, J.; Li, M.; Ding, Z.; Song, Q.; Liao, B.; Fu, L.; Chen, G. Electron Mean-Free-Path Filtering in Dirac Material for Improved Thermoelectric Performance. *Proc. Natl. Acad. Sci. U.S.A.* **2018**, *115* (5), 879–884.
- (20) Gayner, C.; Amouyal, Y. Energy Filtering of Charge Carriers: Current Trends, Challenges, and Prospects for Thermoelectric Materials. *Adv. Funct. Mater.* **2020**, *30* (18), 1901789.
- (21) Moore, J. E. The Birth of Topological Insulators. *Nature* **2010**, 464 (7286), 194–198.
- (22) Hasan, M. Z.; Kane, C. L. Colloquium: Topological Insulators. *Rev. Mod. Phys.* **2010**, 82 (4), 3045–3067.
- (23) Roushan, P.; Seo, J.; Parker, C. V.; Hor, Y. S.; Hsieh, D.; Qian, D.; Richardella, A.; Hasan, M. Z.; Cava, R. J.; Yazdani, A. Topological Surface States Protected from Backscattering by Chiral Spin Texture. *Nature* **2009**, *460* (7259), 1106–1109.
- (24) Fu, L.; Kane, C. L. Topological Insulators with Inversion Symmetry. *Phys. Rev. B* **2007**, *76* (4), 045302.
- (25) Fu, C.; Sun, Y.; Felser, C. Topological Thermoelectrics. *APL Mater.* **2020**, 8 (4), 040913.
- (26) Xu, Y.; Gan, Z.; Zhang, S.-C. Enhanced Thermoelectric Performance and Anomalous Seebeck Effects in Topological Insulators. *Phys. Rev. Lett.* **2014**, *112* (22), 226801.
- (27) Hinsche, N. F.; Zastrow, S.; Gooth, J.; Pudewill, L.; Zierold, R.; Rittweger, F.; Rauch, T.; Henk, J.; Nielsch, K.; Mertig, I. Impact of the Topological Surface State on the Thermoelectric Transport in Sb2Te3 Thin Films. *ACS Nano* **2015**, *9* (4), 4406–4411.
- (28) Heremans, J. P.; Cava, R. J.; Samarth, N. Tetradymites as Thermoelectrics and Topological Insulators. *Nat. Rev. Mater.* **2017**, 2 (10), 17049.
- (29) Shi, H.; Parker, D.; Du, M.-H.; Singh, D. J. Connecting Thermoelectric Performance and Topological-Insulator Behavior: Bi2Te3 and Bi2Te2Se from First Principles. *Phys. Rev. Appl.* **2015**, 3 (1), 014004.
- (30) Xu, N.; Xu, Y.; Zhu, J. Topological Insulators for Thermoelectrics. NPJ. Quantum Mater. 2017, 2 (1), 51.
- (31) Venkatasubramanian, R.; Siivola, E.; Colpitts, T.; O'Quinn, B. Thin-Film Thermoelectric Devices with High Room-Temperature Figures of Merit. *Nature* **2001**, *413* (6856), 597–602.
- (32) Poudel, B.; Hao, Q.; Ma, Y.; Lan, Y.; Minnich, A.; Yu, B.; Yan, X.; Wang, D.; Muto, A.; Vashaee, D.; Chen, X.; Liu, J.; Dresselhaus, M. S.; Chen, G.; Ren, Z. High-Thermoelectric Performance of Nanostructured Bismuth Antimony Telluride Bulk Alloys. *Science* **2008**, 320 (5876), 634–638.
- (33) Tretiakov, O. A.; Abanov, Ar.; Sinova, J. Holey Topological Thermoelectrics. *Appl. Phys. Lett.* **2011**, *99* (11), 113110.
- (34) Osterhage, H.; Gooth, J.; Hamdou, B.; Gwozdz, P.; Zierold, R.; Nielsch, K. Thermoelectric Properties of Topological Insulator Bi2Te3, Sb2Te3, and Bi2Se3 Thin Film Quantum Wells. *Appl. Phys. Lett.* **2014**, *105* (12), 123117.
- (35) Luo, Z.; Liu, H.; Spann, B. T.; Feng, Y.; Ye, P.; Chen, Y. P.; Xu, X. Measurement of In-Plane Thermal Conductivity of Ultrathin Films Using Micro-Raman Spectroscopy. *Nanoscale and Microscale Thermophysical Engineering* **2014**, *18* (2), 183–193.
- (36) Luo, Z.; Maassen, J.; Deng, Y.; Du, Y.; Garrelts, R. P.; Lundstrom, M. S.; Ye, P. D.; Xu, X. Anisotropic In-Plane Thermal Conductivity Observed in Few-Layer Black Phosphorus. *Nat. Commun.* **2015**, *6* (1), 8572.
- (37) Luo, Z.; Tian, J.; Huang, S.; Srinivasan, M.; Maassen, J.; Chen, Y. P.; Xu, X. Large Enhancement of Thermal Conductivity and Lorenz Number in Topological Insulator Thin Films. *ACS Nano* **2018**, *12* (2), 1120–1127.
- (38) Huang, S.; Ghosh, N.; Niu, C.; Chen, Y. P.; Ye, P. D.; Xu, X. Optically Gated Electrostatic Field-Effect Thermal Transistor. *Nano Lett.* **2024**, 24 (17), 5139–5145.
- (39) Pettes, M. T.; Maassen, J.; Jo, I.; Lundstrom, M. S.; Shi, L. Effects of Surface Band Bending and Scattering on Thermoelectric

- Transport in Suspended Bismuth Telluride Nanoplates. *Nano Lett.* **2013**, *13* (11), 5316–5322.
- (40) Locatelli, L.; Rossi, P.; Kumar, A.; Wiemer, C.; Lamperti, A.; Mantovan, R.; Raciti, G.; Xu, K.; Reparaz, J. S.; Caironi, M.; Pace, G. Unleashing the Impact of Topological Surface States on the Thermoelectric Properties of Granular Sb2Te3 Thin Films Deposited on Flexible Substrates. ACS Appl. Mater. Interfaces 2025, 17 (25), 37206–37215.
- (41) Sun, Y.; Cheng, H.; Gao, S.; Liu, Q.; Sun, Z.; Xiao, C.; Wu, C.; Wei, S.; Xie, Y. Atomically Thick Bismuth Selenide Freestanding Single Layers Achieving Enhanced Thermoelectric Energy Harvesting. *J. Am. Chem. Soc.* **2012**, *134* (50), 20294–20297.
- (42) Cahill, D. G.; Watson, S. K.; Pohl, R. O. Lower Limit to the Thermal Conductivity of Disordered Crystals. *Phys. Rev. B* **1992**, 46 (10), 6131–6140.
- (43) McIver, J. W.; Hsieh, D.; Steinberg, H.; Jarillo-Herrero, P.; Gedik, N. Control over Topological Insulator Photocurrents with Light Polarization. *Nat. Nanotechnol.* **2012**, *7* (2), 96–100.
- (44) Junck, A.; Refael, G.; von Oppen, F. Photocurrent Response of Topological Insulator Surface States. *Phys. Rev. B* **2013**, 88 (7), 075144.
- (45) Sun, G. L.; Li, L. L.; Qin, X. Y.; Li, D.; Zou, T. H.; Xin, H. X.; Ren, B. J.; Zhang, J.; Li, Y. Y.; Li, X. J. Enhanced Thermoelectric Performance of Nanostructured Topological Insulator Bi2Se3. *Appl. Phys. Lett.* **2015**, *106* (5), 053102.
- (46) Choe, H. S.; Li, J.; Zheng, W.; Lee, J.; Suh, J.; Allen, F. I.; Liu, H.; Choi, H.-J.; Walukiewicz, W.; Zheng, H.; Wu, J. Anomalously High Electronic Thermal Conductivity and Lorenz Ratio in Bi2Te3 Nanoribbons Far from the Bipolar Condition. *Appl. Phys. Lett.* **2019**, 114 (15), 152101.
- (47) Wu, L.; Brahlek, M.; Valdés Aguilar, R.; Stier, A. V.; Morris, C. M.; Lubashevsky, Y.; Bilbro, L. S.; Bansal, N.; Oh, S.; Armitage, N. P. A Sudden Collapse in the Transport Lifetime across the Topological Phase Transition in (Bi1–xInx)2Se3. *Nat. Phys.* **2013**, *9* (7), 410–414.
- (48) Wu, X.; Li, J.; Ma, X.-M.; Zhang, Y.; Liu, Y.; Zhou, C.-S.; Shao, J.; Wang, Q.; Hao, Y.-J.; Feng, Y.; Schwier, E. F.; Kumar, S.; Sun, H.; Liu, P.; Shimada, K.; Miyamoto, K.; Okuda, T.; Wang, K.; Xie, M.; Chen, C.; Liu, Q.; Liu, C.; Zhao, Y. Distinct Topological Surface States on the Two Terminations of MnBi4Te7. *Phys. Rev. X* 2020, *10* (3), 031013.
- (49) Krishnamoorthy, H. N. S.; Dubrovkin, A. M.; Adamo, G.; Soci, C. Topological Insulator Metamaterials. *Chem. Rev.* **2023**, *123* (8), 4416–4442.
- (50) Huang, S.; Xu, X. Optical Chirality Detection Using a Topological Insulator Transistor. *Adv. Opt. Mater.* **2021**, 9 (10), 2002210.
- (51) Xiong, J.; Petersen, A. C.; Qu, D.; Hor, Y. S.; Cava, R. J.; Ong, N. P. Quantum Oscillations in a Topological Insulator Bi2Te2Se with Large Bulk Resistivity ( $6\Omega$ cm). *Physica E Low Dimens Syst. Nanostruct* **2012**, 44 (5), 917–920.
- (52) Ren, Z.; Taskin, A. A.; Sasaki, S.; Segawa, K.; Ando, Y. Large Bulk Resistivity and Surface Quantum Oscillations in the Topological Insulator Bi2Te2Se. *Phys. Rev. B* **2010**, *82* (24), 241306.
- (53) Cao, H.; Liu, C.; Tian, J.; Xu, Y.; Miotkowski, I.; Hasan, M. Z.; Chen, Y. P. Controlling and Distinguishing Electronic Transport of Topological and Trivial Surface States in a Topological Insulator. *arXiv* 2014, arXiv:1409.3217.
- (54) Roy Chowdhury, P.; Shi, J.; Feng, T.; Ruan, X. Prediction of Bi2Te3-Sb2Te3 Interfacial Conductance and Superlattice Thermal Conductivity Using Molecular Dynamics Simulations. *ACS Appl. Mater. Interfaces* **2021**, *13* (3), 4636–4642.
- (55) Ju, Z.; Crawford, C.; Adamczyk, J.; Toberer, E. S.; Kauzlarich, S. M. Study of the Thermoelectric Properties of Bi2Te3/Sb2Te3 Core—Shell Heterojunction Nanostructures. ACS Appl. Mater. Interfaces 2022, 14 (21), 24886–24896.
- (56) Rashid, Z.; Nissimagoudar, A. S.; Li, W. Phonon Transport and Thermoelectric Properties of Semiconducting Bi2Te2X (X = S, Se, Te) Monolayers. *Phys. Chem. Chem. Phys.* **2019**, *21* (10), 5679–5688.

- (57) Suh, J.; Yu, K. M.; Fu, D.; Liu, X.; Yang, F.; Fan, J.; Smith, D. J.; Zhang, Y.; Furdyna, J. K.; Dames, C.; Walukiewicz, W.; Wu, J. Simultaneous Enhancement of Electrical Conductivity and Thermopower of Bi2Te3 by Multifunctionality of Native Defects. *Adv. Mater.* **2015**, 27 (24), 3681–3686.
- (58) Stanford, M. G.; Pudasaini, P. R.; Belianinov, A.; Cross, N.; Noh, J. H.; Koehler, M. R.; Mandrus, D. G.; Duscher, G.; Rondinone, A. J.; Ivanov, I. N.; Ward, T. Z.; Rack, P. D. Focused Helium-Ion Beam Irradiation Effects on Electrical Transport Properties of Few-Layer WSe2: Enabling Nanoscale Direct Write Homo-Junctions. *Sci. Rep.* **2016**, *6* (1), 27276.
- (59) Bouteiller, H.; Burcea, R.; Poterie, C.; Fournier, D.; Giovannelli, F.; Nyman, J.; Ezzahri, Y.; Dubois, S.; Eklund, P.; le Febvrier, A.; Barbot, J.-F. Improving the Thermoelectric Performance of Scandium Nitride Thin Films by Implanting Helium Ions. *Commun. Mater.* **2025**, *6* (1), 30.
- (60) Wiendlocha, B. Resonant Levels, Vacancies, and Doping in Bi2Te3, Bi2Te2Se, and Bi2Se3 Tetradymites. *J. Electron. Mater.* **2016**, 45 (7), 3515–3531.
- (61) Huang, S.; Miotkowski, I.; Chen, Y. P.; Xu, X. Deep Tuning of Photo-Thermoelectricity in Topological Surface States. *Sci. Rep.* **2020**, 10 (1), 16761.
- (62) Niu, C.; Huang, S.; Ghosh, N.; Tan, P.; Wang, M.; Wu, W.; Xu, X.; Ye, P. D. Tunable Circular Photogalvanic and Photovoltaic Effect in 2D Tellurium with Different Chirality. *Nano Lett.* **2023**, 23 (8), 3599–3606.
- (63) Hosur, P. Circular Photogalvanic Effect on Topological Insulator Surfaces: Berry-Curvature-Dependent Response. *Phys. Rev. B* **2011**, 83 (3), 035309.
- (64) Park, K.; Heremans, J. J.; Scarola, V. W.; Minic, D. Robustness of Topologically Protected Surface States in Layering of Bi2Te3 Thin Films. *Phys. Rev. Lett.* **2010**, *105* (18), 186801.
- (65) M, S.; Amirthapandian, S.; Magudapathy, P.; Srivastava, S. K.; Asokan, K. Tuning of the Thermoelectric Properties of Bi2Te3 Nanorods Using Helium Ion Irradiation. *ACS Omega* **2018**, 3 (12), 18411–18419.
- (66) Tian, J.; Miotkowski, I.; Hong, S.; Chen, Y. P. Electrical Injection and Detection of Spin-Polarized Currents in Topological Insulator Bi2Te2Se. *Sci. Rep.* **2015**, *5* (1), 14293.
- (67) Okada, K. N.; Ogawa, N.; Yoshimi, R.; Tsukazaki, A.; Takahashi, K. S.; Kawasaki, M.; Tokura, Y. Enhanced Photogalvanic Current in Topological Insulators via Fermi Energy Tuning. *Phys. Rev. B* **2016**, *93* (8), 081403.
- (68) Hsiung, T.-C.; Mou, C.-Y.; Lee, T.-K.; Chen, Y.-Y. Surface-Dominated Transport and Enhanced Thermoelectric Figure of Merit in Topological Insulator Bi1.5 Sb0.5Te1.7Se1.3. *Nanoscale* **2015**, 7 (2), 518–523.
- (69) Tang, H.; Wang, X.; Xiong, Y.; Zhao, Y.; Zhang, Y.; Zhang, Y.; Yang, J.; Xu, D. Thermoelectric Characterization of Individual Bismuth Selenide Topological Insulator Nanoribbons. *Nanoscale* **2015**, 7 (15), 6683–6690.
- (70) Gayner, C.; Natanzon, Y.; Kauffmann, Y.; Amouyal, Y. Topologically-Enhanced Thermoelectric Properties in Bi2Te3-Based Compounds: Effects of Grain Size and Misorientation. ACS Appl. Mater. Interfaces 2022, 14 (44), 49730–49745.